Unbiased CLEAN for STIX in Solar Orbiter

The Astrophysical Journal Supplement Series, 268:68 (10pp), 2023 October https://doi.org/10.3847/1538-4365/acf669

Unbiased CLEAN for STIX in Solar Orbiter

Emma Perracchione[1], Fabiana Camattari[1,2], Anna Volpara[3], Paolo Massa[4], Anna Maria Massone[3], and Michele Piana[3,5]
[1] Dipartimento di Scienze Matematiche "Giuseppe Luigi Lagrange", Politecnico di Torino, Corso Duca degli Abruzzi, 24, I-10129, Torino, Italy
emma.perracchione@polito.it
[2] Dipartimento di Matematica "Giuseppe Peano", Università di Torino, Via Carlo Alberto 10, I-10123, Torino, Italy
[3] MIDA, Dipartimento di Matematica, Università di Genova, via Dodecaneso 35, I-16145 Genova, Italy
[4] Department of Physics and Astronomy, Western Kentucky University, Bowling Green, KY 42101, USA
[5] Istituto Nazionale di Astrofisica, Osservatorio Astrofisico di Torino, Pino Torinese, Italy
Received 2023 August 1; revised 2023 August 30; accepted 2023 September 2; published 2023 October 12

Abstract

CLEAN is an iterative deconvolution method for radio and hard-X-ray solar imaging. In a specific step of its pipeline, CLEAN requires the convolution between an idealized version of the instrumental point-spread function (PSF), and a map collecting point sources located at positions from where most of the flaring radiation is emitted. This step has highly heuristic motivations and the shape of the idealized PSF, which depends on the user's choice, impacts the shape of the reconstruction. This study introduces a user-independent release of CLEAN for image reconstruction from observations recorded by the Spectrometer/Telescope for Imaging X-rays (STIX) on board Solar Orbiter. Specifically, we show here that this unbiased release of CLEAN outperforms the standard version of the algorithm, with reconstructions in line with the ones offered by other imaging methods developed in the STIX framework.

Unified Astronomy Thesaurus concepts: Solar x-ray flares (1816); Astronomy image processing (2306); X-ray telescopes (1825); Interdisciplinary astronomy (804)

1. Introduction

Native measurements in both radio astronomy (Thompson et al. 2017) and modern hard-X-ray solar imaging (Piana et al. 2022) are sets of spatial Fourier components of the incoming source flux, named visibilities, measured at specific spatial frequency samples, named (u, v) points. In both radio astronomy and hard-X-ray solar imaging, CLEAN (Högbom 1974; Schmahl et al. 2007) is a nonlinear image reconstruction algorithm that iteratively deconvolves the instrumental point-spread function (PSF) from the so-called dirty map, i.e., the discretized inverse Fourier transform of the experimental visibility set. More specifically, the CLEAN algorithm is made of a CLEAN loop, which generates the following: a set of CLEAN components located at the points of the solar disk from where most of the source emission propagates; an estimate of the background; the convolution of the CLEAN components map with an idealized PSF, named the CLEAN beam; and, eventually, the CLEANed map, i.e., the sum of the outcome of this convolution step with the convolved background residuals.

In the framework of the visibility-based NASA RHESSI (Lin et al. 2002), CLEAN has been by far the most utilized image reconstruction method. However, we are now in the Solar Orbiter (Müller et al. 2020) era and other image reconstruction methods besides CLEAN are currently used for the analysis of the hard-X-ray visibilities recorded by the Spectrometer/Telescope for Imaging X-rays (STIX) on board the ESA cluster (Krucker et al. 2020). This is due to the fact that novel imaging algorithms have been introduced (Massa et al. 2020; Volpara et al. 2022; Perracchione et al. 2021a; Siarkowski et al. 2020; Duval-Poo et al. 2018; Felix et al. 2017), which are characterized by notable reliability and by an automation degree higher than the one offered by CLEAN. In fact, the step of the iterative scheme that requires the convolution of the CLEAN components map with the CLEAN beam significantly depends on the user's choice, since the functional shape of the CLEAN beam (e.g., its FWHM) is typically designed according to heuristic motivations. This results in CLEANed maps of the same event that are often characterized by different properties, while conservative choices of the CLEAN beam's FWHM often lead to underresolved reconstructions with correspondingly high χ^2 values.

The objective of the present paper is to introduce and validate a completely user-independent technique for the exploitation of the CLEAN components associated with the analysis of STIX visibilities. In particular, we show here that the feature augmentation process introduced by Perracchione et al. (2021b) and applied to RHESSI experimental and STIX synthetic visibilities can lead to an unbiased version of CLEAN (u-CLEAN), in which the convolution between the CLEAN components map and the idealized PSF is replaced by an automated interpolation/extrapolation procedure. Further, u-CLEAN does not need any addition of residuals, since the resulting reconstructed map is automatically embedded in the emission background. In this study we show how the u-CLEAN pipeline works in the case of STIX observations and compare its outcomes with the reconstructions provided by other imaging methods contained in the STIX ground software. We point out that the u-CLEAN reconstructions presented in this paper can also be interpreted as the first maps provided by the augmented uv_smooth algorithm introduced by Perracchione et al. (2021a) in the case of experimental STIX visibilities.

The plan of the paper is as follows. Section 2 sets up the formalism of CLEAN and points out the need of an unbiased release of the iterative algorithm. Section 3 introduces the novel automated version of CLEAN exploiting feature augmentation. Section 4 applies u-CLEAN to STIX observations and assesses its performances. Our conclusions are offered in Section 5.

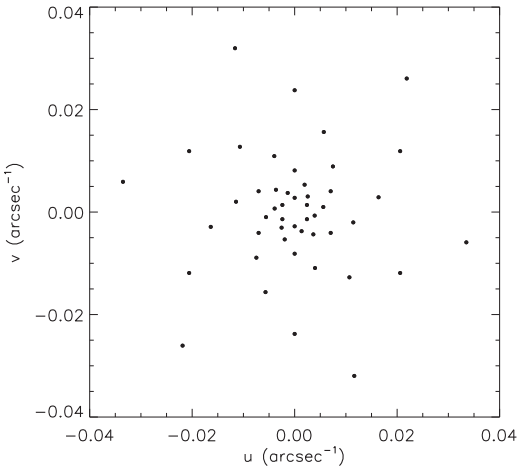

Figure 1. Sampling of the spatial frequency (u, v)-plane realized by the 30 STIX collimators, which have been duplicated by exploiting the symmetry properties of the Fourier transform, i.e., we also consider the complex conjugates of the 30 STIX visibility samples.

2. Toward Unbiased CLEAN

The STIX imaging concept (Massa et al. 2023) relies on Moiré patterns (Prince et al. 1988) generated by 30 subcollimators that detect photons from the Sun in the energy range between a few keV and around 100 keV. These raw data are then transformed into a set of $n = 60$ visibilities that sample the spatial frequency domain, the (u, v)-plane, according to the spirals in Figure 1. Since visibilities can be seen as spatial Fourier components of the incoming photon flux, the STIX imaging problem reads as

$$\boldsymbol{V} = \boldsymbol{F}\boldsymbol{f}, \tag{1}$$

where $\boldsymbol{f}$ is the vector whose components are the discretized values of the incoming flux, $\boldsymbol{F}$ is the discretized Fourier transform sampled at the set $\{\boldsymbol{u}_k = (u_k, v_k)\}_{k=1}^n$, and $\boldsymbol{V}$ is the complex vector of the observed visibilities.

Given $\boldsymbol{x} = (x, y)$ in the image domain, visibility-based CLEAN iteratively solves the convolution equation

$$\hat{\boldsymbol{f}}(\boldsymbol{x}) = (K * \boldsymbol{f})(\boldsymbol{x}) := \iint K(\boldsymbol{x} - \boldsymbol{x}')\boldsymbol{f}(\boldsymbol{x}')d\boldsymbol{x}' , \tag{2}$$

where $\boldsymbol{f}$ is the unknown source flux, K is the so-called dirty beam, i.e., the instrumental PSF

$$K(\boldsymbol{x}) = \sum_{k=1}^{n} \exp(-2\pi i \boldsymbol{x} \cdot \boldsymbol{u}_k)\delta\boldsymbol{u}_k, \tag{3}$$

and $\hat{\boldsymbol{f}}$ is the so-called dirty map

$$\hat{\boldsymbol{f}}(\boldsymbol{x}) = \sum_{k=1}^{n} \boldsymbol{V}_k \exp[-2\pi i(\boldsymbol{x} \cdot \boldsymbol{u}_k)]\delta\boldsymbol{u}_k, \tag{4}$$

i.e., the inverse Fourier transform of the visibilities. In both Equations (3) and (4) $\delta\boldsymbol{u}_k = (\delta u_k, \delta v_k)$, $k = 1, \ldots, n$, denote the weights in the numerical integration.

CLEAN steps are summarized in a schematic way in Algorithm 1. The automation of the CLEAN loop (Step 2) is guaranteed by a stopping rule that applies when the "Dirty Map Update" step returns just experimental noise. Instead, Step 4 of the pipeline, i.e., the construction of the CLEANed map, is clearly ambiguous and mostly biased by the user's decision about the shape of the CLEAN beam K^C. In the version of the CLEAN code originally developed for RHESSI (Schmahl et al. 2007), this convolution kernel is modeled by a two-dimensional Gaussian function whose FWHM is chosen by the user according to heuristic rules of thumb. This convolution product is the main reason for the low photometric reliability of the CLEANed map, while conservative choices for FWHM typically lead to under-resolved reconstructions, with correspondingly high χ^2 values.

In order to solve this issue, u-CLEAN replaces Step 3 and Step 4 of the CLEAN pipeline by a feature augmentation and a soft thresholding step, both characterized by a high degree of automation.

3. u-CLEAN via Feature Augmentation

The u-CLEAN approach is based on interpolating the experimental visibilities with a basis that depends on the CLEAN components map, and on inverting the interpolated visibility surface by means of an iterative constrained algorithm. Specifically, any interpolant, namely P, has the property of matching the given measured visibilities at the corresponding locations (the (u, v) points), i.e.,

$$P(\boldsymbol{u}_k) = \boldsymbol{V}_k = (\Re(\boldsymbol{V}_k), \Im(\boldsymbol{V}_k)), \quad k = 1,\ldots,n. \tag{5}$$

If the interpolation method is mesh-free, as in our case, P consists of a linear combination of n linearly independent basis functions $\{B_1(\boldsymbol{u}),\ldots,B_n(\boldsymbol{u})\}$ and can be written as

$$P(\boldsymbol{u}) = \sum_{k=1}^{n} (a_k + i\, b_k)B_k(\boldsymbol{u}) , \tag{6}$$

where the coefficients $\{a_k\}_{k=1}^n$ and $\{b_k\}_{k=1}^n$ are determined thanks to the interpolation conditions (5).

Algorithm 1. CLEAN Steps

Inputs: Sampling points $\{\boldsymbol{u}_k = (u_k, v_k)\}_{k=1}^n$; visibility vector $\boldsymbol{V}$; gain factor γ; CLEAN beam K^C.

Outputs: The CLEANed map $\overline{\boldsymbol{f}}$, the CLEAN components map $\tilde{\boldsymbol{f}}$, the convolved residual map $K^C{*}\boldsymbol{f}^B$, the dirty map $\hat{\boldsymbol{f}}$, and the CLEANed map without background residuals $K^C{*}\tilde{\boldsymbol{f}}$.

1: **Initialization.**

a. **Dirty map:**

$$\hat{\boldsymbol{f}}^{(0)}(\boldsymbol{x}) = \sum_{k=1}^{n} \boldsymbol{V}_k \exp[-2\pi i(\boldsymbol{x} \cdot \boldsymbol{u}_k)]\delta\boldsymbol{u}_k.$$

b. **Dirty beam:**

$$K(\boldsymbol{x}) = \sum_{k=1}^{n} \exp(-2\pi i \boldsymbol{x} \cdot \boldsymbol{u}_k)\delta\boldsymbol{u}_k.$$

c. **CLEAN component map:** $\tilde{\boldsymbol{f}}^{(0)}(\boldsymbol{x}) = \boldsymbol{0}$.

2: **CLEAN loop** $(t \geqslant 1)$.

a. **Maximum identification:**

$$\boldsymbol{x}_{\max}^{(t)} = \arg\max_{\boldsymbol{x}} \hat{\boldsymbol{f}}^{(t-1)}(\boldsymbol{x}), \quad \hat{\boldsymbol{f}}_{\max}^{(t)} = \hat{\boldsymbol{f}}^{(t-1)}(\boldsymbol{x}_{\max}^{(t)}).$$

b. **CLEAN components update:**

$$\tilde{\boldsymbol{f}}^{(t)}(\boldsymbol{x}) = \tilde{\boldsymbol{f}}^{(t-1)}(\boldsymbol{x}) + \frac{\gamma \hat{\boldsymbol{f}}_{\max}^{(t)}}{\max_{\boldsymbol{x}}|K(\boldsymbol{x})|}\delta(\boldsymbol{x} - \boldsymbol{x}_{\max}^{(t)}) .$$

c. **Dirty map update:**

$$\hat{\boldsymbol{f}}^{(t)}(\boldsymbol{x}) = \hat{\boldsymbol{f}}^{(t-1)}(\boldsymbol{x}) - \frac{\gamma \hat{\boldsymbol{f}}_{\max}^{(t)}}{\max_{\boldsymbol{x}}|K(\boldsymbol{x})|}K(\boldsymbol{x} - \boldsymbol{x}_{\max}^{(t)}).$$

3: **Estimate of the background map:**

$$\boldsymbol{f}^B(\boldsymbol{x}) \simeq \frac{\hat{\boldsymbol{f}}(\boldsymbol{x})}{T},$$

where $\hat{\boldsymbol{f}}$ is the result of the final dirty map update and T is an estimate of the integral of the PSF over the field of view. 4:

4: **Construction of the CLEANed map:**

$$\overline{\boldsymbol{f}}(\boldsymbol{x}) = (K^C{*}(\tilde{\boldsymbol{f}} + \boldsymbol{f}^B))(\boldsymbol{x}) = (K^C{*}\tilde{\boldsymbol{f}})(\boldsymbol{x}) + (K^C{*}\boldsymbol{f}^B)(\boldsymbol{x}),$$

where $\tilde{\boldsymbol{f}}$ is the result of the final CLEAN components update, and $K^C(\boldsymbol{x})$ is the so-called CLEAN beam, i.e., an idealized version of the PSF.

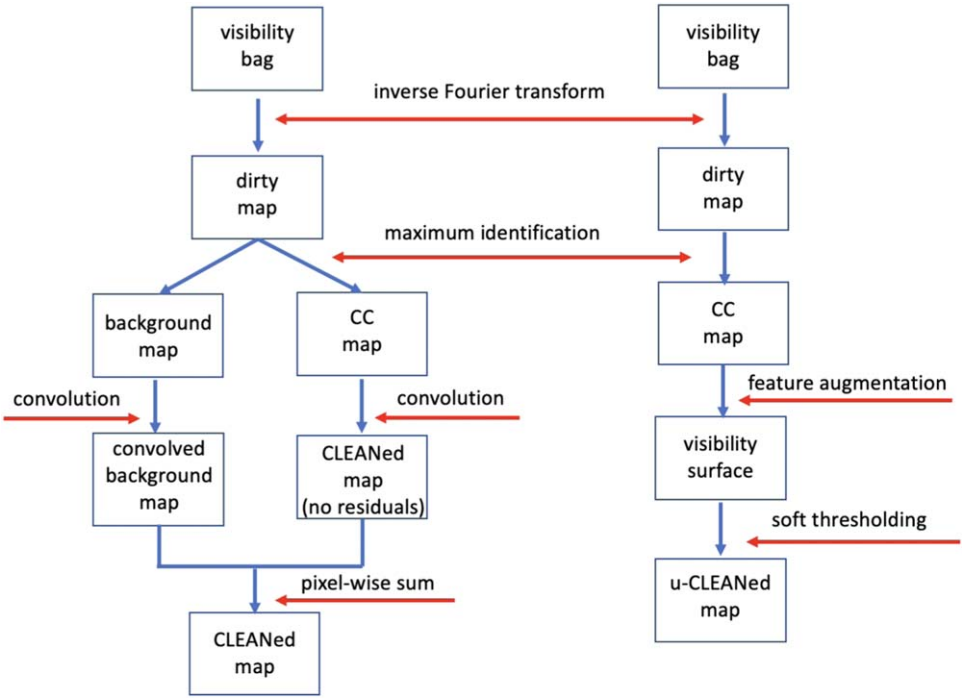

Figure 2. The CLEAN and u-CLEAN pipelines.

Hence, in our case, $P(\boldsymbol{u})$ approximates the unknown value of the visibility at any given query point $\boldsymbol{u} = (u, v)$. By taking a grid of query points, the final output of the interpolation procedure will be an $N \times N$ visibility surface grid, with $N \gg n$.

In our interpolation procedure we will take advantage of feature augmentation schemes (Bozzini et al. 2015). Their basic idea consists of the construction of enriched data sets obtained by concatenating the original data with other features that include prior information. In other words, we consider the transformed set of data $\{\boldsymbol{u}_k^{\Psi} = (u_k, v_k, \Psi(u_k, v_k))\}_{k=1}^{n}$, where, for this specific task, $\Psi\colon \mathbb{C} \to \mathbb{C}$ depends on the CLEAN components map. Specifically, given the CLEAN components map, namely $\tilde{\boldsymbol{f}}$, which provides a very preliminary knowledge on the flaring source, we define the function Ψ by applying forward to $\tilde{\boldsymbol{f}}$ the Fourier operator in Equation (1), i.e., we get an $N \times N$ grid $\tilde{\boldsymbol{V}}$. Hence, we simply define the scaling function Ψ as the so-computed grid $\tilde{\boldsymbol{V}}$. Finally, our interpolant will be of the form

$$\begin{aligned} \overline{\boldsymbol{V}} &:= P(\boldsymbol{u}^{\Psi}) = P((u, v, \Psi(u, v))) \\ &= \sum_{k=1}^{n} (a_k + i\, b_k) B_k(u, v, \Psi(u, v)), \end{aligned} \tag{7}$$

with $\Psi \equiv \tilde{\boldsymbol{V}}$ and where our basis $\{B_1(\boldsymbol{u}^{\Psi}),\ldots,B_n(\boldsymbol{u}^{\Psi})\}$ is given by the so-called variably scaled kernels, e.g., Gaussians or Matérn radial basis functions (Bozzini et al. 2015; De Marchi et al. 2020). Hence, the u-CLEAN interpolation basis integrates the CLEAN components map via the function Ψ.

Figure 2 compares the CLEAN and u-CLEAN pipelines, pictorially showing the higher simplicity of the latter. Further, the new steps in u-CLEAN are completely user-independent: feature augmentation is just an interpolation process, while soft thresholding is a standard projected Landweber scheme (Piana & Bertero 1997) that just needs the choice of an initialization (in the current implementation of u-CLEAN we have chosen $\overline{\boldsymbol{f}}^{(0)} = \boldsymbol{0}$) and the application of and a stopping rule that relies on a check on the χ^2 values (Allavena et al. 2012).

Algorithm 2. u-CLEAN Steps

Inputs: Sampling points $\{\boldsymbol{u}_k = (u_k, v_k)\}_{k=1}^{n}$; visibility vector $\boldsymbol{V}$; gain factor γ.
Outputs: The u-CLEANED map $\overline{\boldsymbol{f}}$.
1: **Initialization:** same as in Algorithm 1.
2: **CLEAN loop**: same as in Algorithm 1.
3: **Feature augmentation:** generate the visibility surface
$$\overline{\boldsymbol{V}} := P(\boldsymbol{u}^{\Psi}) = P((u, v, \Psi(u, v))) = \sum_{k=1}^{n} (a_k + i\, b_k) B_k(u, v, \Psi(u, v)), \quad \text{with } \Psi \equiv \tilde{\boldsymbol{V}}.$$
4: **Soft thresholding:**
$$\overline{\boldsymbol{f}}^{(k+1)} = \mathcal{P}_{+}\overline{\boldsymbol{f}}^{(k+1)},$$
where $\overline{\boldsymbol{f}}^{(k+1)}$ is computed as in (9).

More formally, the plain application of the inverse Fourier transform on the interpolated data would imply several drawbacks, such as ringing effects on the reconstructed image, and hence we rely on the use of constrained inversion techniques. Indeed, let us denote by χ_D the characteristic function on the disk D defined by the STIX visibilities as in Figure 1; a band-limited approximation of the (unknown) solution of the imaging problem is given by

$$\overline{\boldsymbol{f}} = \overline{\boldsymbol{F}}^{-1}(\chi_D\, \overline{\boldsymbol{V}}), \tag{8}$$

where $\overline{\boldsymbol{F}}$ is the $N^2 \times N^2$ discretized Fourier transform and $\overline{\boldsymbol{f}}$ and $\chi_D\, \overline{\boldsymbol{V}}$ are $N^2 \times 1$ vectors. An extrapolation out of the band D can be computed via the projected Landweber iteration according to the following rule: given the characteristic function χ_D of D, and a relaxation parameter $\tau \in [0, 1]$, compute

$$\overline{\boldsymbol{F}}\,\overline{\boldsymbol{f}}^{(k+1)} = \tau \overline{\boldsymbol{F}}\,\overline{\boldsymbol{f}} + (1 - \tau\, \chi_D)\overline{\boldsymbol{F}}\,\overline{\boldsymbol{f}}^{(k)}, \tag{9}$$

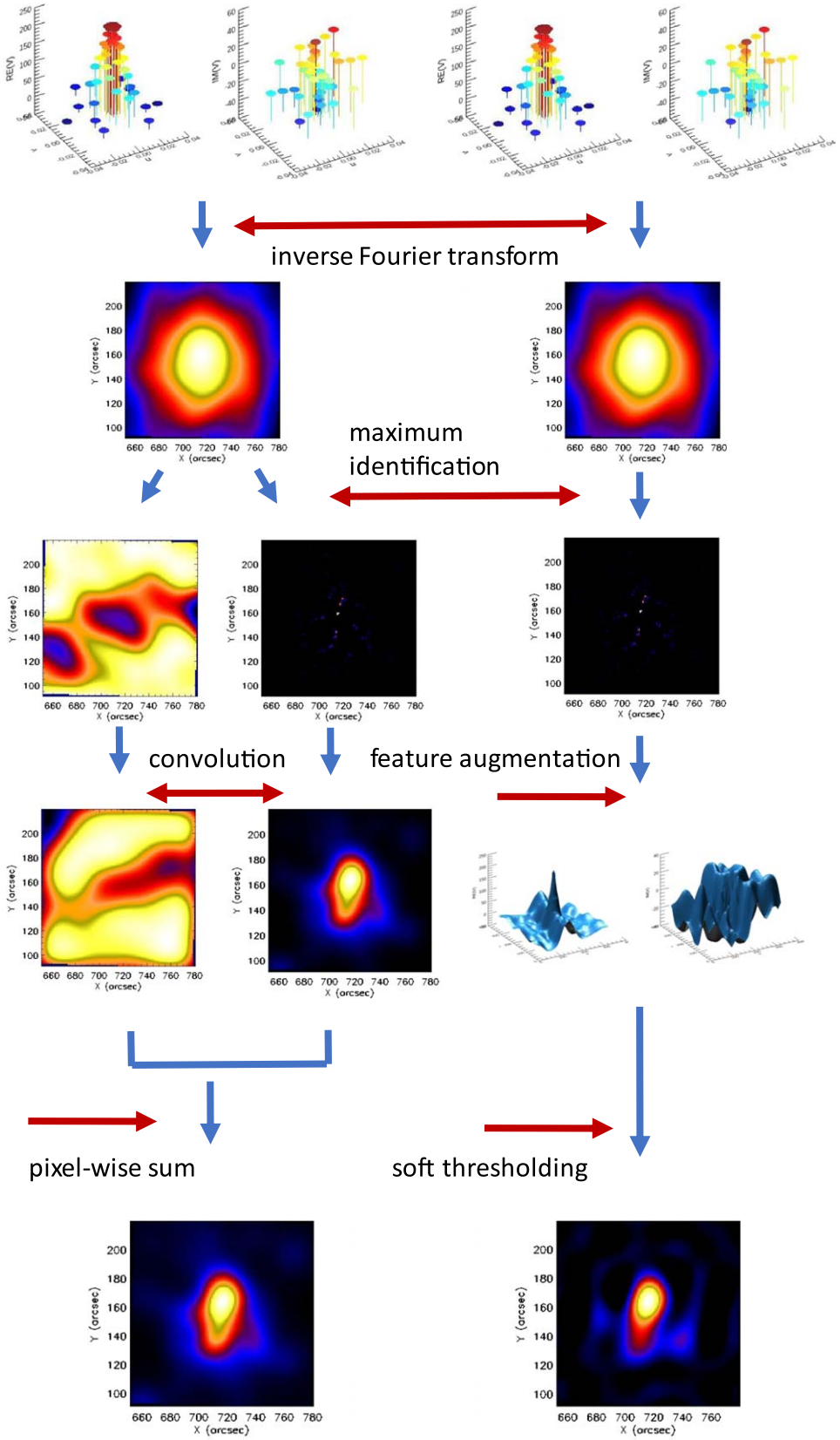

Figure 3. Results of the application of the CLEAN and u-CLEAN pipelines to the STIX visibility bags associated with the 2022 November 11 flare in the time range between 01:30:15 and 01:30:45 UT, for the energy channel between 5 and 9 keV.

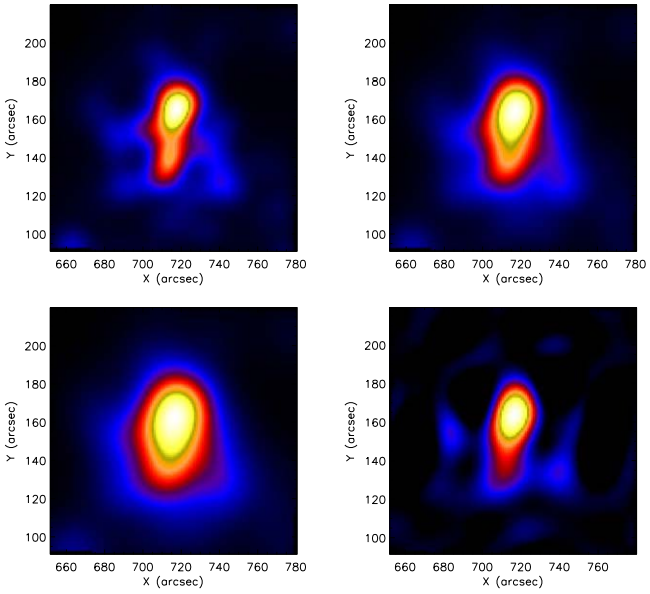

Figure 4. Reconstruction of the 2022 November 11 flare in the time range between 01:30:15 and 01:30:45 UT. Top-left panel: CLEANed map with FHWM equal to 15″; top-right panel: CLEANed map with FWHM equal to 20″ (default value); bottom-left panel: CLEANed map with FWHM equal to 25″; bottom-right panel: u-CLEANed map.

with $k = 1, 2, \ldots$, and apply the nonnegativity constraint by means of the projection

$$\overline{\boldsymbol{f}}^{(k+1)} = \mathcal{P}_+ \overline{\boldsymbol{f}}^{(k+1)}, \tag{10}$$

where $\mathcal{P}_+$ pixel-wise imposes a positivity constraint, i.e., it returns zero for each negative pixel value. The computation of $\overline{\boldsymbol{f}}^{(k+1)}$ is realized by applying a fast Fourier transform–based routine, and we have set $\tau = 0.2$ (but the scheme is not very sensitive with respect to the choice of this parameter). For further details, we refer the reader to the u-CLEAN pipeline that is sketched in Algorithm 2.

4. Application to STIX Visibilities

As a case study we considered the event that occurred on 2022 November 11 and, at first, we focused on the thermal energy channel 5–9 keV and on the time range from 01:30:15 to 01:30:45 UT.[6] The results of the application of CLEAN and u-CLEAN to the visibility bags associated with this event are illustrated in Figure 3, which reproduces the scheme of Figure 2 and where, this time, each box contains the actual product of the corresponding computational step. Figure 4 compares the reconstruction provided by u-CLEAN with three CLEANed maps obtained by using three different values of the FWHM for the CLEAN beam. Figure 5 contains the fits of the experimental visibilities provided by the CLEAN components map, the CLEANed map, and the reconstruction provided by u-CLEAN, respectively. The CLEANed map has been obtained by using the default value of 20″ for the CLEAN beam FWHM, and such a value will be used in all the experiments if not otherwise stated.

We point out that, in the CLEAN pipeline of Figure 3, the residual map (left panel after "maximum identification") corresponds to the final iteration of the "Dirty Map Update."

[6] Throughout the paper, times are in Solar Orbiter UT.

We also notice that the two panels after "feature augmentation" in the u-CLEAN pipeline correspond to the real and imaginary parts of the interpolated visibility surface.

Figure 4 compares the reconstruction provided by u-CLEAN with three reconstructions provided by CLEAN in the case of three increasing values of the FWHM in the final convolution step. Table 1 contains the reconstructed parameters associated with these four maps and with the CLEAN components map. The mean and standard deviations in this table are obtained by perturbing the visibilities according to Volpara et al. (2022). The parameters associated with the maximum of the flux are rather similar for all reconstructions, while CLEAN photometry decreases with increasing FWHM values. However, these fluxes are always higher than the ones provided by the CLEAN components map and u-CLEAN, which suggests that CLEAN overestimates the overall photometry. Consistently, the χ^2 value corresponding to u-CLEAN is better than the ones associated with the three CLEAN reconstructions.

The second experiment compares the u-CLEAN performances to the ones provided by other reconstruction methods in the case of some flaring events observed by STIX in both the thermal and nonthermal regimes. Specifically, we considered

1. The 2021 May 8 event in the time range between 18:24:00 and 18:32:00 UT, in the thermal channel between 6 and 10 keV.
2. The same event as before in the same time interval but, this time, in the nonthermal channel between 18 and 28 keV.
3. The 2020 June 7 event in the time range between 21:39:00 and 21:42:49 UT and in the thermal range between 6 and 10 keV.
4. The 2022 March 31 event in the time interval between 18:26:20 and 18:27:00 UT and in the nonthermal energy range between 25 and 50 keV.

The reconstructions of these flaring sources are represented in Figures 6–9, and have been obtained by means of MEM_GE (Massa et al. 2020), VIS_FWDFIT_PSO (Volpara et al. 2022), CLEAN, and u-CLEAN, respectively. The χ^2 values and the corresponding reconstructed parameters are contained in Tables 2 and 3. We point out that, in the thermal cases, VIS_FWDFIT_PSO utilizes an elliptical Gaussian function as an input model, and that, for all cases, FWHM in CLEAN is set to the default value of 20″. These experiments show that MEM_GE and u-CLEAN provide similar results in terms of both fitting reliability and overall morphology. In particular, in Figure 7 the reconstructions provided by the two methods nicely follow the loop shape of the source. Further, the foot points in Figure 9 are probably overresolved by MEM_GE and underresolved by CLEAN, while VIS_FWDFIT_PSO and u-CLEAN provide similar results. The parameters in Tables 2 and 3 confirm that CLEAN tends to overestimate the overall flux in the reconstruction, with all flux values being higher than the ones provided by the other methods. This is even more evident if we consider Table 3, where the CLEANed map overestimates the total flux and underestimates the fluxes emitted by the two sources (calculated by cropping the image with two circles of diameter equal to 25″ around the center of each source). The overestimation of the total flux by CLEAN is due to the added residuals, which increase the value of the background emission. Conversely, the total flux of each source is underestimated since the final convolution with the CLEAN

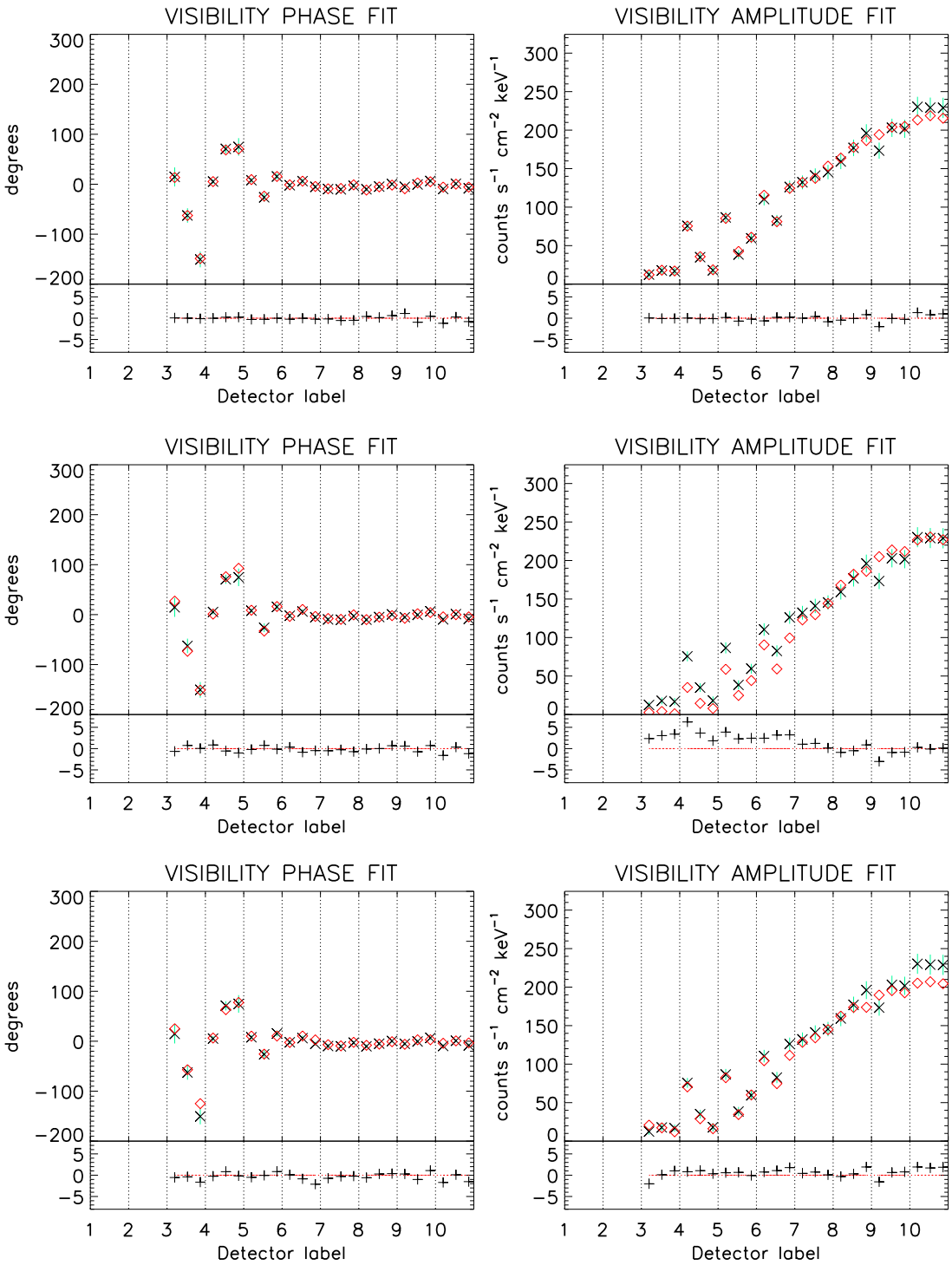

Figure 5. Top to bottom: comparison between the experimental visibilities in the case study of 2022 November 11, the visibilities predicted by the CLEAN components map, and by the images reconstructed with CLEAN and u-CLEAN, respectively. In the top plot of each panel, the black crosses represent the experimental values of the visibility phases (left column) or amplitudes (right column), the green bars represent the associated uncertainties, and the red diamonds denote the values of the visibility phases or amplitudes predicted from the reconstructed image. In the bottom plot of each panel, the black pluses represent the residuals (computed as the difference between the observed values and the predicted ones normalized by the corresponding uncertainty), while the red horizontal dashed line denotes the "zero" value as a reference.

beam distributing the flux far away from each peak. Coherently, the same behavior occurs to the FWHM values, while the χ^2 values are consistently higher in CLEAN. u-CLEAN is able to determine the source positions close to the values provided by VIS_FWDFIT_PSO, which is, by construction, the imaging method that best fits the source position. Also, the χ^2 values predicted by u-CLEAN are almost always very close to the ones associated with MEM_GE, which is so far probably the reference reconstruction method in the STIX community.

Table 1
Imaging Parameters and χ^2 Values for the Reconstructions of the 2022 November 11 Flare in the Time Range between 01:30:15 and 01:30:45 UT

	x_p (arcseconds)	y_p (arcseconds)	FWHM (arcseconds)	Flux (counts cm^{-2} s^{-1} keV^{-1})	χ^2
CCs	715.9 ± 0.3	158.4 ± 0.3	2.4 ± 0.6	223 ± 7	0.70
CLEAN (FWHM 15)	717.2 ± 0.4	164.8 ± 0.8	25.2 ± 0.6	265 ± 11	5.03
CLEAN (FWHM 20)	716.9 ± 0.2	163.8 ± 0.7	32.3 ± 0.6	246 ± 9	6.92
CLEAN (FWHM 25)	716.2 ± 0.4	161.9 ± 0.6	38.5 ± 0.6	236 ± 8	11.04
u-CLEAN	715.9 ± 0.2	163.1 ± 0.7	23.8 ± 0.7	219 ± 9	2.08

Note. The results are provided by the CLEAN components map (CCs), CLEAN (for three different values of FWHM measured in arcseconds), and u-CLEAN. The flare location is denoted as (x_p, y_p) while the flux is measured in counts cm^{-2} s^{-1} keV^{-1}.

Table 2
Imaging Parameters and χ^2 Values Predicted by MEM_GE, VIS_FWDFIT_PSO, the CLEAN Components Map (CCs), the CLEANed Map (with FWHM Equal to the Default Value of 20″) and by u-CLEAN

Method	x_p (arcseconds)	y_p (arcseconds)	FWHM (arcseconds)	Flux (counts cm^{-2} s^{-1} keV^{-1})	χ^2
	2021 May 8, 6–10 keV				
MEM_GE	620.2 ± 0.3	315.8 ± 0.4	18.9 ± 0.6	124 ± 6	2.75
VIS_FWDFIT_PSO	620.9 ± 0.4	314.8 ± 0.4	20.8 ± 0.3	108 ± 2	5.66
CCs	$621.0887 \pm 3 \times 10^{-4}$	$315.5845 \pm 3 \times 10^{-4}$	1.13 ± 0.00	110 ± 4	3.97
CLEAN	$621.0887 \pm 3 \times 10^{-4}$	$315.5845 \pm 3 \times 10^{-4}$	26.3 ± 0.3	134 ± 6	32.5
u-CLEAN	$620.0887 \pm 3 \times 10^{-4}$	$315.5845 \pm 3 \times 10^{-4}$	21.6 ± 0.3	115 ± 4	4.75
	2021 May 8, 18–28 keV				
MEM_GE	613.6 ± 13.3	312.3 ± 13.6	12 ± 1	0.6 ± 0.1	2.96
VIS_FWDFIT_PSO	616.3 ± 0.9	311.8 ± 0.8	19 ± 2	0.48 ± 0.02	3.29
CCs	616.7 ± 0.6	313.0 ± 0.7	1.5 ± 0.3	0.42 ± 0.03	2.84
CLEAN	616.5 ± 0.7	313.1 ± 0.6	26 ± 1	0.7 ± 0.1	4.04
u-CLEAN	615 ± 1	313.8 ± 0.8	22 ± 1	0.64 ± 0.05	3.19
	2020 June 7, 6–10 keV				
MEM_GE	-1595.1 ± 0.6	-793 ± 2	27 ± 2	15.2 ± 0.5	1.73
VIS_FWDFIT_PSO	-1592.3 ± 0.2	$-792.2633 \pm 6 \times 10^{-4}$	36 ± 1	13.5 ± 0.3	4.38
CCs	-1594.2 ± 0.2	$-793.2633 \pm 6 \times 10^{-4}$	1.5 ± 0.4	13.6 ± 0.4	0.99
CLEAN	-1594.6 ± 0.6	-795.4 ± 0.9	34 ± 1	16.2 ± 0.9	3.22
u-CLEAN	-1596.2 ± 0.5	-795.9 ± 0.8	26.6 ± 0.8	13.9 ± 0.8	1.72

Note. The cases of the 2021 May 8 and 2020 June 7 events are shown. For the May 8 event, both the thermal channel between 6 and 10 keV and the nonthermal one between 18 and 28 keV are considered. The flare location is denoted as (x_p, y_p) while the flux is measured as counts cm^{-2} s^{-1} keV^{-1}.

5. Comments and Conclusions

Although CLEAN is a reference tool for image reconstruction in hard-X-ray solar physics, its reliability and degree of automation are significantly limited by the final convolution step involving the CLEAN components map and an idealized model for the instrument PSF, and by the need to a posteriori add a background estimate to the result of this deconvolution. These two rather heuristic steps may imply underresolved CLEANed maps, with unrealistically high χ^2 values, and an unsatisfactory automation level for the overall algorithm. Therefore, the present study exploits the CLEAN components map to generate an interpolated visibility surface, and applies soft thresholding to reconstruct an unbiased CLEAN map in the image space, starting from STIX observations. The resulting u-CLEAN is an iterative scheme characterized by a high degree of automation and by reconstruction performances in line with respect to the ones provided by other imaging methods developed for STIX. u-CLEAN is now at disposal for testing

Table 3
Imaging Parameters and χ^2 Values Predicted by MEM_GE, VIS_FWDFIT_PSO, the CLEAN Components Map (CCs), the CLEANed Map, and by u-CLEAN in the Case of the 2022 March 31 Event

	Source 1				Source 2					
	x_p (arcseconds)	y_p (arcseconds)	FWHM (arcseconds)	Flux counts (cm^{-2} s^{-1}) (keV^{-1})	x_p (arcseconds)	y_p (arcseconds)	FWHM (arcseconds)	Flux (counts cm^{-2} s^{-1} keV^{-1})	Total Flux (counts cm^{-2} s^{-1} keV^{-1})	χ^2
MEM_GE	-2231 ± 1	560.3 ± 0.8	12.8 ± 0.9	1.66 ± 0.05	-2207.7 ± 0.8	478.8 ± 0.8	12.9 ± 0.9	1.56 ± 0.09	6.0 ± 0.4	3.99
VIS_FWDFIT_PSO	-2232.9 ± 0.6	559.3 ± 0.8	15.3 ± 0.8	2.5 ± 0.1	-2209.3 ± 0.7	478.8 ± 0.8	14 ± 2	2.35 ± 0.09	5.6 ± 0.2	5.26
CCs	-2232.8 ± 0.6	559.7 ± 0.6	1.8 ± 0.3	2.1 ± 0.1	-2208.5 ± 0.8	478.6 ± 0.7	1.9 ± 0.3	1.9 ± 0.1	5.6 ± 0.4	1.96
CLEAN	-2232.6 ± 0.6	560.7 ± 0.5	23.0 ± 0.6	1.65 ± 0.07	-2207.5 ± 0.5	479.3 ± 0.6	22.4 ± 0.6	1.51 ± 0.09	10 ± 2	11.6
u-CLEAN	-2233.8 ± 0.6	561.6 ± 0.7	18.6 ± 0.5	2.7 ± 0.2	-2208.0 ± 0.8	479.7 ± 0.8	18.6 ± 0.3	1.8 ± 0.1	6.6 ± 0.3	6.17

Note. The footpoint centers are denoted as (x_p, y_p) while the flux is measured as counts cm^{-2} s^{-1} keV^{-1}.

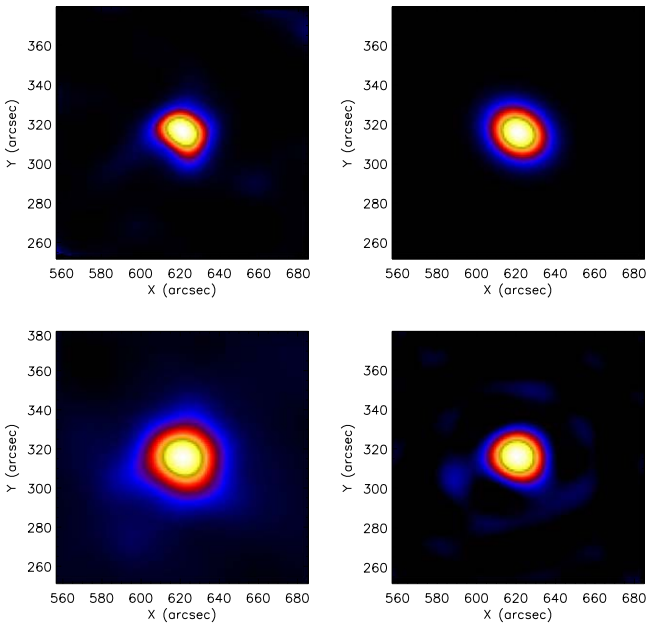

Figure 6. Reconstructions of the the 2021 May 8 event in the energy range 6–10 keV provided by MEM_GE (top left), VIS_FWDFIT_PSO (top right), CLEAN (bottom left), and u-CLEAN (bottom right).

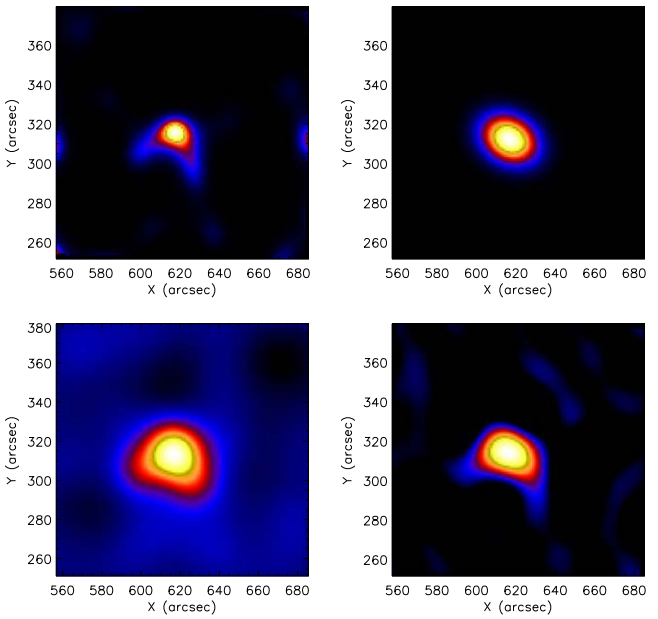

Figure 7. Reconstructions of the 2021 May 8 event in the energy range 18–28 keV provided by MEM_GE (top left), VIS_FWDFIT_PSO (top right), CLEAN (bottom left), and u-CLEAN (bottom right).

(Perracchione et al. 2023). Further, we believe that a multiscale extension is of a rather straightforward implementation. Finally, we point out that u-CLEAN can be interpreted as the first release of the feature-augmented uv_smooth tailored to the case of STIX visibilities.

Acknowledgments

Solar Orbiter is a space mission of international collaboration between ESA and NASA, operated by ESA. The STIX instrument is an international collaboration between Switzerland, Poland, France, Czech Republic, Germany, Austria, Ireland, and Italy. A.M.M., A.V., and M.P. are supported by the "Accordo ASI/INAF Solar Orbiter: Supporto scientifico per la realizzazione degli strumenti Metis, SWA/DPU e STIX nelle Fasi D-E." E.P. and A.M.M. acknowledge the support of the Fondazione Compagnia di San Paolo within the framework of the Artificial Intelligence Call for Proposals, AIxtreme project (ID Rol: 71708). A.M.M. is also grateful to the HORIZON Europe ARCAFF Project, grant No. 101082164.

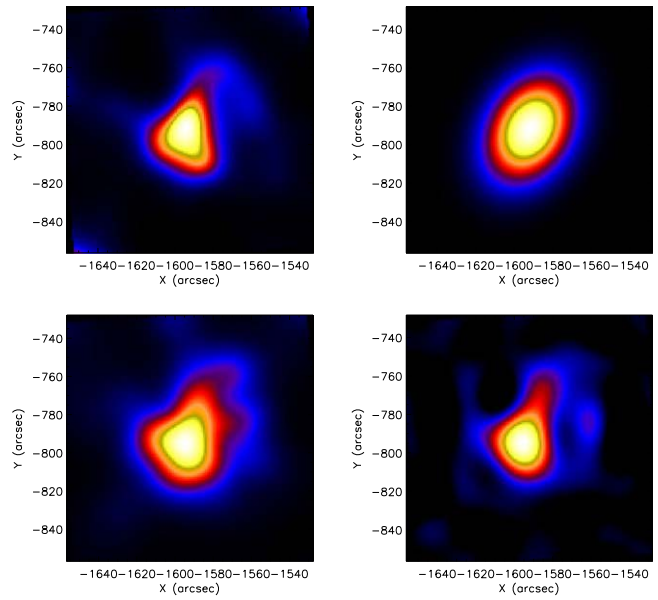

Figure 8. Reconstructions of the 2020 June 7 event in the energy range 6–10 keV provided by MEM_GE (top left), VIS_FWDFIT_PSO (top right), CLEAN (bottom left), and u-CLEAN (bottom right).

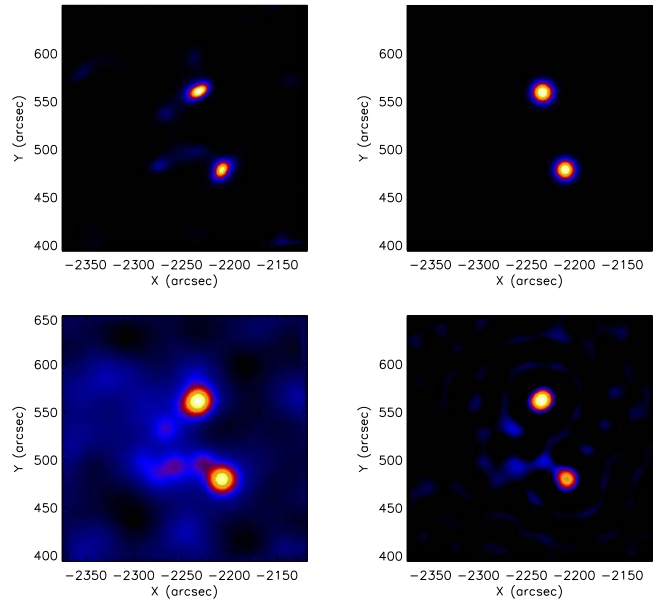

Figure 9. Reconstructions of the 2022 March 31 event in the energy range 25–50 keV provided by MEM_GE (top left), VIS_FWDFIT_PSO (top right), CLEAN (bottom left), and u-CLEAN (bottom right).

ORCID iDs

Emma Perracchione https://orcid.org/0000-0003-2663-7803
Michele Piana https://orcid.org/0000-0003-1700-991X

References

Allavena, S., Piana, M., Benvenuto, F., & Massone, A. M. 2012, Inverse Probl. Imag., 6, 147
Bozzini, M., Lenarduzzi, L., Rossini, M., & Schaback, R. 2015, IJNA, 35, 199
De Marchi, S., Erb, W., Marchetti, F., Perracchione, E., & Rossini, M. 2020, SJSC, 42, B472
Duval-Poo, M. A., Piana, M., & Massone, A. M. 2018, A&A, 615, A59
Felix, S., Bolzern, R., & Battaglia, M. 2017, ApJ, 849, 10
Högbom, J. A. 1974, A&AS, 15, 417
Krucker, S., Hurford, G. J., Grimm, O., et al. 2020, A&A, 642, A15
Lin, R., Dennis, B., Hurford, G., et al. 2002, SoPh, 210, 3
Massa, P., Hurford, G. J., Volpara, A., et al. 2023, arXiv:2303.02485
Massa, P., Schwartz, R., Tolbert, A., et al. 2020, ApJ, 894, 46
Müller, D., St, Cyr, O. C., Zouganelis, I., et al. 2020, A&A, 642, A1
Perracchione, E., Camattari, F., Volpara, A., et al., 2023, theMIDAgroup/U-CLEAN: U-CLEAN v0.1.0, valpha, Zenodo, doi:10.5281/zenodo.8269723
Perracchione, E., Massa, P., Massone, A. M., & Piana, M. 2021a, ApJ, 919, 133
Perracchione, E., Massone, A. M., & Piana, M. 2021b, InvPr, 37, 105001
Piana, M., & Bertero, M. 1997, InvPr, 13, 441
Piana, M., Emslie, A. G., Massone, A. M., & Dennis, B. R. 2022, Hard X-Ray Imaging of Solar Flares (Cham: Springer)
Prince, T. A., Hurford, G. J., Hudson, H. S., & Crannell, C. J. 1988, SoPh, 118, 269
Schmahl, E., Pernak, R., Hurford, G., Lee, J., & Bong, S. 2007, SoPh, 240, 242
Siarkowski, M., Mrozek, T., Sylwester, J., Litwicka, M., & Dabek, M. 2020, OAst, 29, 220
Thompson, A., Moran, J., & Swenson, G. 2017, Interferometry and Synthesis in Radio Astronomy (Berlin: Springer)
Volpara, A., Massa, P., Perracchione, E., et al. 2022, A&A, 668, A145